第37卷 第2期 焊 接 学 报 Vol. 37 No. 2
2016年2月 TRANSACTIONS OF THE CHINA WELDING INSTITUTION February 2016

焊接电参数对GTAW熔透状态的影响

张 刚，樊 丁，石 玗，黄健康，李春玲
(兰州理工大学 省部共建有色金属先进加工与再利用国家重点实验室，兰州 730050)

摘 要：针对非熔化极气体保护焊(gas tungsten arc welding，GTAW)过程中因焊接参数波动、热传导条件变化难以实时检测和控制熔透的难题，考虑304不锈钢相变潜热随温度的变化，建立了焊接电参数与熔池相变潜热、背面熔宽间的动态变化数学模型，仿真研究了改变焊接电流、电弧电压对焊缝熔透状态的动态影响规律，预测了恒定电参数下点焊熔透状态发生改变的时间. 采集了同参数焊接过程中表征熔透状态变化的反射激光点阵视频图像，统计计算了实际熔透发生改变的时间. 结果表明，所建立的动态数学模型能够反映焊缝熔透状态随电参数的动态变化过程，且焊接电流对熔透状态的影响更显著；熔透变化预测时间与实测时间一致.

关键词：非熔化极气体保护焊；焊接电参数；建模仿真；熔透
中图分类号：TG 409 **文献标识码**：A **文章编号**：0253－360X(2016)02－0025－04

0 序 言

随着焊接结构向高参数、精密化方向发展，对其焊接质量提出了更高要求，尤其作为评价质量优劣的指标之一焊缝全熔透提出了精确控制要求，但如何在线测量熔透状态是精确控制熔透保证焊接质量的关键和难点问题.

近些年，研究者们采用温度场检测技术[1]、红外成像技术[2]、电弧声[3]、机器视觉[4]、结构激光[5]、熔池振荡频率检测[6]等传感方法对弧焊过程中全熔透状态检测及控制进行了相关研究，并取得了一些显著的成绩，但现有的熔透检测及控制方法中都弱化了焊接电参数对熔透状态的直接作用. 因此，间接获取的表征熔透状态的物理量结果不准确，控制效果不理想. 文中在考虑304不锈钢熔融金属相变潜热随温度变化的条件下，建立了GTAW焊接电参数(焊接电流，电弧电压)与熔池相变潜热、背面熔宽间的动态变化数学模型，仿真研究了变焊接电参数的背面熔宽动态响应规律，预测了恒定电参数下点焊熔透状态发生改变时间，同时采集了相同参数下反映熔透状态变化的反射激光点阵视频图像，通过人工统计分析自动分帧视频图像，获得了实际熔透改变的时间，并与理论预测时间进行了对比. 研究结果为相同焊接热输入、复杂焊况下的熔透控制提供理论参考，缩短焊接试验周期.

收稿日期：2014－01－14
基金项目：973前期研究专项项目(2014CB660810)；国家自然科学基金资助项目(61365011)；陇原创新性人才扶持计划项目；兰州理工大学红柳杰出人才培养计划项目(J201201)

1 动态变化数学模型

考虑液态金属相变潜热是一温度的函数，假定直流GTAW焊接熔池形成、凝固过程中单位时间内输入工件的电弧热量提供固态金属熔化所需的相变潜热和熔融金属凝固所需的能量，因此，焊接电参数与金属相变潜热、熔池体积间存在以下关系，即

$$\eta \cdot Q = \Delta H(T) \cdot V \tag{1}$$

式中：η 表示电弧热效率；Q 表示单位时间内焊件热输入量；$\Delta H(T)$ 表示 T 温度的熔融金属焓变；V 表示熔池体积.

在焊接过程中母材金属熔化和固化时的相变潜热可用随温度变化的热焓值来描述. 焓值的变化 ΔH 可表示为材料密度 ρ，比热容 c 和温度 T 的函数，参数间存在下述关系，即

$$\Delta H(T) = \int_{T_0}^{T} \rho c(T)\,\mathrm{d}T \tag{2}$$

式中：T_0 为工件初始温度.

GTAW稳定焊接时电弧负载电压为阳极压降、阴极和弧柱压降区三部分电压之和. 在焊接参数一定时，阳极压降和阴极压降保持恒定，弧柱压降可表示为电弧弧长和电弧等效电阻的函数. 电弧负载方程可采用Ayrton方程[7]表示为

$$U_a = U_0 + I \cdot R_a + (K_1 + K_2 \cdot I) \cdot l \tag{3}$$

单位时间内焊接电弧热输入可表示为

$$Q = U_a \cdot I = U_0 \cdot I + I^2 \cdot R_a + (K_1 + K_2 \cdot I) \cdot l \cdot I \tag{4}$$

式中: U_a 表示电弧电压; U_0 表示阳极压降和阴极压降之和; R_a 表示电弧等效电阻; K_1, K_2 表示弧长影响系数; l 表示弧长; I 为焊接电流.

根据熔透状态的变化过程(局部熔透—全熔透—过熔透)采用图 1 来描述熔池几何形状.

当未熔透时,熔池形状采用一直径为 W_S 的半球体来近似,此时焊缝熔深 h 与球体半径相等,采用式(5)计算液态金属体积. 当工件熔透或过熔透(熔池正面宽度与背面宽度近似相等)时,采用截面圆锥来近似熔池形状,此时随着焊接热输入的增加,背面熔宽逐渐增加,采用式(6)计算体积.

$$V = \frac{1}{2} \cdot \frac{4\pi}{3} \cdot \left(\frac{W_S}{2}\right)^3 \tag{5}$$

$$V = \frac{\pi}{12} \cdot h \cdot \left(W_s^2 + W_s \cdot W_b + W_b^2\right) \tag{6}$$

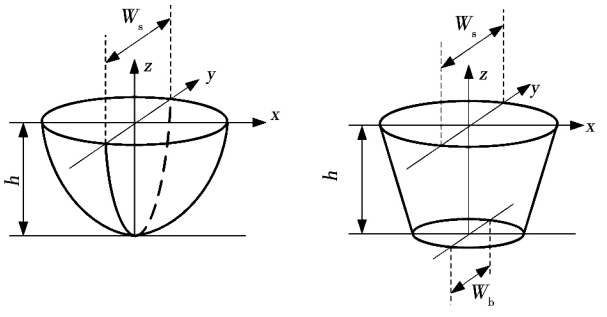

(a) 未熔透型 (b) 熔透型

图 1 熔池几何形状模型

Fig. 1 Geometry model of weld pool

式中: W_S 是正面熔宽; W_b 为背面熔宽; h 为熔深.

以上五式经推导可得到全焊接过程中焊接电参数与熔池正面、背面熔宽间的数学关系表达式为

$$\eta \cdot \left[U_0 I + I^2 \cdot R_a + \left(K_1 + K_2 \cdot I\right) \cdot l \cdot I\right] = \begin{cases} \int_{T_0}^{T} \rho c(T)\,\mathrm{d}T \times \frac{1}{2} \cdot \frac{4\pi}{3} \cdot \left(\frac{W_S}{2}\right)^3 & (W_b = 0) \\ \int_{T_0}^{T} \rho c(T)\,\mathrm{d}T \times \frac{\pi}{12} \cdot h \cdot \left(W_s^2 + W_s \cdot W_b + W_b^2\right) & (W_b \neq 0) \end{cases} \tag{7}$$

2 电参数对熔透状态影响的动态仿真

2.1 焊接电流对熔透状态的作用仿真

根据 Miettinen、Richter 和 Kim[8] 的试验数据,对未知温度范围内的 304 不锈钢比热值进行了插值计算,列出了 0 ~ 1 400 ℃范围内比热容与温度的关系式,即

$$c(T) = 0.5117 \times 10^{-3} + 0.1417 \cdot T \times 10^{-6} \tag{8}$$

基于 Matlab/Simulink 平台采用表 1[9] 仿真参数、ode3(Bogacki-Shampine)算法,固定步长 0.001 s 和已建立的焊接电参数与背面熔宽间的数学模型对 GTAW 点焊过程中熔池几何尺寸随焊接电流的变化进行了仿真分析. 设定仿真 8 s 时焊接电流从 40 A 阶跃到 70 A,弧长保持不变,电流变化如图 2a 所示,随着焊接电弧热输入的积累,点焊过程中熔池背面、正面熔宽及焊缝熔深变化分别如图 2b,c,d.

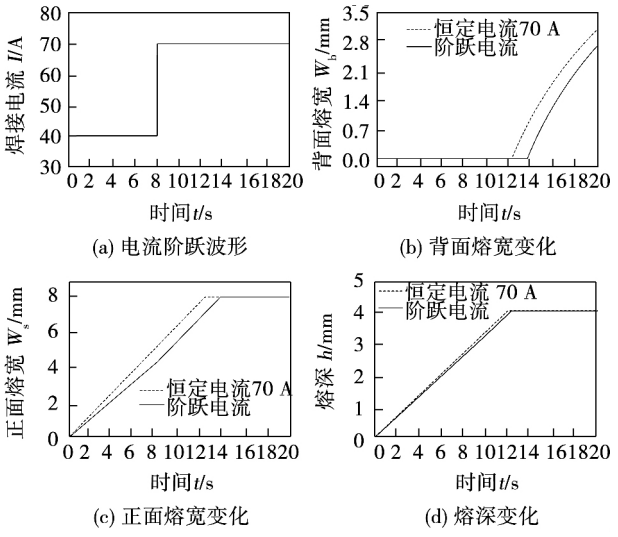

(a) 电流阶跃波形 (b) 背面熔宽变化

(c) 正面熔宽变化 (d) 熔深变化

图 2 不同焊接电流作用的熔池几何尺寸仿真结果

Fig. 2 Simulated geometry results of weld pool under different welding currents

表 1 仿真参数

Table 1 Simulation parameters

母材		阴、阳极压降之和	电弧等效电阻	弧长影响系数	弧长影响系数	热效率系数	初始温度	材料密度
材料	板厚 H/mm	U_o/V	R_a/Ω	K_1/(V·m^{-1})	K_2/(V·m^{-1})	η(%)	T_0/℃	ρ/(g·cm^{-3})
304 不锈钢	4	17	0.02	130	1.2	0.68	20	7.98

当焊接电流从 40 A 阶跃至 70 A 后,随电弧热输入,弧柱直径的增大,工件熔深、熔池正面熔宽都增大;但电弧潜入工件深度的增加使得电弧斑点移动范围受限,因此正面熔宽增大速率较小、熔深增加

速率较大,反映在图 2c 和 2d 中第 8 ~ 14 s 的实直线斜度略大于 0 ~ 8 s 时间段内的实直线斜度. 观察图 2b,2c,2d 发现,焊接到第 14 s 时,工件开始被熔透,背面熔宽逐渐增加,正面熔宽和熔深基本保持不变. 观察实际焊接过程发现,当工件被熔透时,焊缝背面熔宽增加的速率远大于正面熔宽的增加,但因背面熔宽的增加,液态金属体积增大,重力和电弧压力作用下,熔池表面凹陷,焊缝背面出现凸出,因此整体焊缝熔深基本不变. 为进一步验证文中熔池几何参数随焊接电流变化模型的准确性,将恒定电流和变焊接电流下的仿真结果进行了对比分析. 结果表明,恒定电流 70 A 的前 8 s 焊接过程中电弧对工件的热输入积累明显高于 40 A 的,使工件提前 2 s 达到完全熔透状态(图 2b). 从图 2c 和 2d 实虚线可见,增加焊接电流能更迅速的增加电弧热输入使熔池几何尺寸变化更明显,表现在曲线斜率的变化.

2.2　电弧电压对熔透状态的作用仿真

在恒定电流下通过改变弧长来改变电弧电压仿真研究了熔深、熔宽随电弧电压的动态响应规律. 采用表 1 参数,焊接电流为 70 A. 结果如图 3 所示.

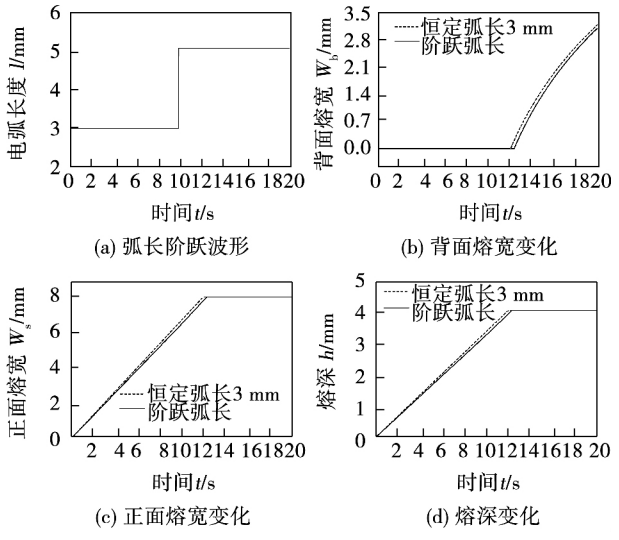

图 3　不同弧长作用的熔池几何尺寸仿真结果

Fig. 3　Simulated geometry results of weld pool under different arc lengths

分析图 3a 可知,第 10 s 弧长从 3 mm 阶跃到 5 mm 后,随电弧被拉长,电弧电压增大,电弧功率增加,但电弧热源半径增大,电弧散热增加,使输入工件的能量密度减小,因此阶跃弧长下的熔宽、熔深增加速率相对恒定 3 mm 弧长的较小,反映在图 3c,3d 中 0 ~ 10 s 实直线斜率略大于 10 ~ 12 s 实直线斜率,但基本成一直线. 而且,较短弧长下电弧能量密度更集中,工件热输入积累效果更明显,更容易焊透工件(图 3b). 对比图 2b 和图 3b,图 2d 和图 3d 发现,焊透相同板厚的工件增大焊接电流比增大弧长所需时间短即焊接电流对工件热输入的作用要高于弧长作用,因此可采用调节焊接热输入来控制焊缝熔透状态,焊接电流对焊缝熔透作用更显著.

3　仿真结果验证

通过对 GTAW 焊缝熔透检测与控制研究可知,焊缝由局部熔透达到完全熔透时,熔池自由表面塌陷量由正变负(假定表面凸出为正,凹陷为负);当处于过熔透时,熔池表面塌陷量随背面熔宽的增加而迅速增加,并且不同熔透状态所对应的反射激光点阵形态区别很明显[5]. 因此采用表 1 参数,4 mm 恒定弧长和 70 A 恒定电流进行了点焊试验,利用采样率 30 Hz 的 CCD 摄像机实时获取了焊接 20 s 的反射激光点阵视频图像,并将不同熔透状态的熔池表面进行了三维恢复,典型反射激光点阵图像和三维恢复结果如图 4 所示. 通过分析图 4 熔池表面高度变化,获得了局部熔透到完全熔透的临界点图像. 分析统计 20 s 内采集的 600 帧自动分帧反射激光

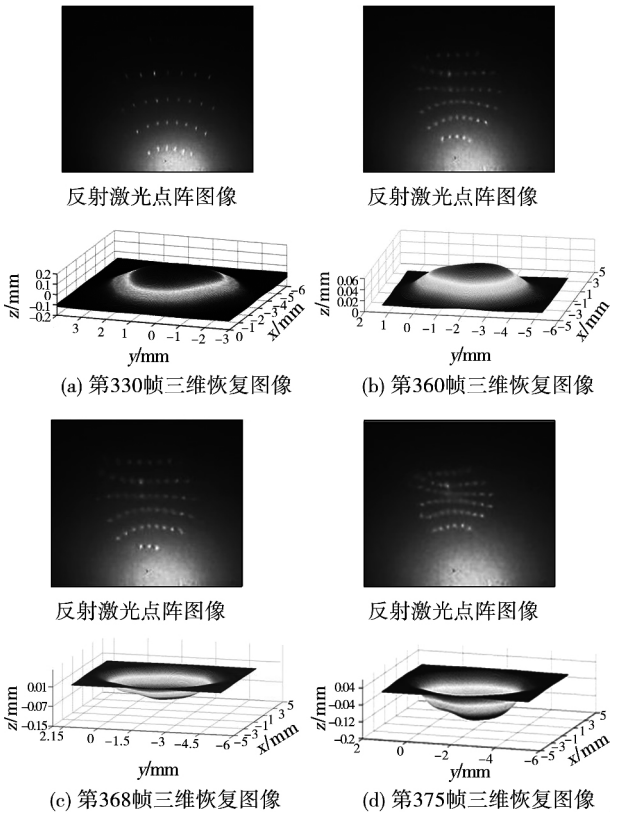

图 4　不同熔透状态下的激光点阵形态及三维恢复结果

Fig. 4　Shapes of reflected laser dots and three dimensional reconstructed weld pool under different weld penetrations

点阵图像可知，在70 A焊接电流作用下，焊缝达到全熔透状态时，熔池表面高度近乎为零，约对应为第360帧反射激光点阵图像，由此可获得熔透状态改变约需要焊接12 s. 最后求解该条件下所建立的数学模型获得的计算值为12 s，由此证明文中所建立的数学模型可较好的反映焊接过程中熔宽、熔深随焊接热输入的变化过程，可理论预测某一恒定焊接电流下工件熔透状态改变所所需时间，也可预测获得一定体积的熔池所需的焊接电流或电弧电压.

4 结 论

(1) 考虑304不锈钢相变潜热随温度变化条件下，建立了焊接电参数与熔池相变潜热、背面熔宽间的动态变化数学模型，并改变焊接电参数对熔池几何形状参数的动态影响进行了仿真. 结果表明，该数学模型能够反映焊接电参数对熔透状态的作用规律，且焊接电流对熔透状态的作用更显著.

(2) 对比分析点焊试验熔透状态改变实测时间与理论计算时间表明，文中条件下达到全熔透状态约需焊接12s，验证了所建模型的合理性和准确性.

参考文献:

[1] 张 华，潘际銮，廖宝剑. 焊接温度场的实时检测与熔透闭环控制[J]. 焊接学报，1998，19(3)：176－183.
Zhang Hua，Pan Jiluan，Liao Baojian. Real-time measurement of welding temperature field and closed-loop control of penetration [J]. Transactions of the China Welding Institution，1998，19(3)：176－183.

[2] Chokkalingham S，Chndrasekhar N，Vasudevan M. Predicting the depth of penetration and weld bead width from the infrared thermal image of the weld pool using artificial neural network modeling [J]. Journal of Intelligent Manufacturing，2012，23(5)：1995－2001.

[3] Pal K，Pal S. Monitoring of weld penetration using arc acoustics [J]. Materials and Manufacturing Processes，2011，26(5)：684－693.

[4] 郑 军，潘际銮. 基于被动视觉的焊接过程多信息检测系统[J]. 焊接学报，2010，31(11)：49－52.
Zheng Jun，Pan Jiluan. Multi-information detection system of welding process based on passive vision [J]. Transactions of the China Welding Institution，2010，31(11)：49－52.

[5] Zhang YM，Song H S. Monitoring and control of penetration in GTAW and pipe welding [J]. Welding Journal，2013，92(9)：190s－196s.

[6] 杨春利，张九海，王其隆. TIG焊熔池外激谐振与熔透的关系[J]. 焊接学报，1990，11(4)：193－198.
Yang Chunli，Zhang Jiuhai，Wang Qilong. Relationship between the weld pool resonance and the weld full penetration in TIG welding [J]. Transactions of theChina Welding Institution，1990，11(4)：193－198.

[7] Choi J H，Lee J Y，Yoo C D. Simulation of dynamic behavior in a GMAW system [J]. Welding Journal，2001，80(10)：239－245.

[8] Artermis A. Thermal and solidification modeling of weld：a design tool approach [D]. US，Tufts University，2002.

[9] Thomsen J S. Advanced control methods for optimization of arc welding [D]. Aalborg，Aalborg University，2005.

作者简介： 张 刚，男，1986年出生，博士研究生. 主要从事焊接过程控制及机器人自动化方面的研究工作. 发表论文10余篇. Email：berscheid@126.com

通讯作者： 樊 丁，男，教授，博士研究生导师. Email：fand@lut.cn

[上接第4页]

Zhang Yongzhong，Xi Mingzhe，Shi Likai. Multi-layer functional gradient materials of 316LSS to stellite 31 alloy prepared by laser clad deposition [J]. Heat Treatment of Metals，2007，32(9)：45－47.

[10] Wang X L，Wang G F，Zhang K F. Effect of mechanical alloying on microstructure and mechanical properties of hot-pressed Nb-16Si alloy [J]. Materials Science and Engineering A，2010，527：3253－3258.

[11] Feng J C. Interfacial reaction mechanism in solid state bonded SiC ceramic/metal (Ti，Cr，Nb and Ta) joint [D]. Japan，Osaka University，1995.

[12] Park J S，Landry K，Perepezko J H. Kinetic control of silicon carbide/metal reactions [J]. Materials Science and Engineering. 1999，A259：279－286.

[13] Shuster J C. Design criteria and limitations for SiC-metal and Si_3N_4-metal joints derived from phase diagram studies of the systems Si-C-metal and Si-N-metal. structural ceramics joining Ⅱ [C] // Ceramic Transactions，Westerville，Ohio：Amerian Ceramics Soc，1993，43－57.

[14] Okamoto H. Nb-Si (Niobium-Silicon) [J]. Journal of Phase Equilibria and Diffusion，2005，26(6)：649－650.

[15] Liermann H P，Singh A K，Somayazulu M，*et al*. Compression behavior of NbC under nonhydrostatic conditions to 57 GPa [J]. International Journal of Refractory Metals & Hard Materials，2007，25：386－391.

作者简介： 李胜男，女，1988年出生，硕士研究生. 研究方向为新型的先进连接技术及3D打印. 发表论文1篇. Email：lishengnan621@163.com

通讯作者： 熊华平，男，研究员. Email：xionghuaping69@sina.cn

ing, Ministry of Education, Wuhan University of Technology, Wuhan 430070, China). pp 17 – 20

Abstract: A metallization packaging technology for fiber Bragg grating (FBG) vibration sensor was investigated in the paper, including surface metallization and laser welding packaging of FBG. The FBGs and fiber ends were pre-plated with sliver by magnetron sputtering method, and then plated with nickel by electrolytic plating. Finally, the plated components were packaged in the sensor structure through laser welding to shape a fully metalized packaged FBG sensor. To verify the effect of FBG vibration sensor metallization packaging, the performance of sensors were tested and compared to that of sensors with epoxy package. It was found that the resonant frequency increased by 50% to 1495Hz, the acceleration sensitivity decreased by 15% to about 60 mV/ms^{-2}, the linear measurement range increased about 20% up to 12 m/s^2, the repeatability error was less than 4.7%, and the matching state of double FBGs did not vary with temperature. The results show that the metalized packaging method is feasible for FBG sensors and can improve their performance and long-term stability.

Key words: FBG vibration sensor; metalized package; magnetron sputter plating; laser welding

Effect of rare earth Y_2O_3 on abrasion resistance of 6063 Al laser cladding Ni-based cladding layer WANG Chenglei, ZHANG Guangyao, GAO Yuan, WEI Wenzhu, LU Xiaohui (Guilin University of Electronic Technology, Guilin 541004, China). pp 21 – 24, 37

Abstract: Ni60 alloy cladding layer with different contents of rare earth Y_2O_3 was prepared on the surface of 6063 aluminum alloys using laser cladding technology, and the wear resistance of cladding layers was investigated. By analyzing the microstructure of cladding layers, the surface morphology of grinding cracks, wear loss and friction coefficient, the effect of Y_2O_3 contents on the wear resistance of laser cladding Ni-based coating was studied. The results show that Ni60 cladding layer with 5% Y_2O_3 displayed significant network distribution of dendrites and fine equiaxed grains. The rare earth Y_2O_3 could improve the microstructure of Ni60 cladding layer on the surface of aluminum alloy, promote grains refinement and uniform distribution of composition. The chipping degree of wear surface was smaller on Ni60 cladding layers with Y_2O_3 than on Ni60 cladding layer, and the friction stability were improved. With increasing the content of rare earth, the amount of wear loss decreased, but the wear loss did not change substantially when the Y_2O_3 content was higher than 5%. Ni60 cladding layer with 5% Y_2O_3 had better wear morphology, lower wear loss and more stable friction coefficient, and its wear resistance was 6.1 times of that of Ni60 cladding layer and 20.1 times of that of 6063 Al alloy matrix.

Key words: laser cladding; rare earth; nickel-based; wear

Effect of welding electric parameters on weld penetration of GTAW ZHANG Gang, FAN Ding, SHI Yu, HUANG Jiankang, Li Chunling (State Key Laboratory of Advanced Processing and Recycling Non-ferrous Metals, Lanzhou University of Technology, Lanzhou 730050, China). pp 25 – 28

Abstract: To investigate the influence of welding electric parameters, heat transfer conditions on detection and control of weld penetration in gas tungsten arc welding process, a new mathematical model of welding electric parameters and latent heat, backside weld width in GTAW process was established by considering latent heat varying with temperature for 304 stainless steel. The effect of welding current and arc voltage on weld penetration was simulated, and the time of complete penetration was predicted under constant welding current in spot welding. To verify the accuracy and effectiveness of established model, a series of experiments were conducted and the laser dots images reflecting the dynamic variation of weld penetration were captured. After statistically analyzing and calculating the variable time of reflected dots shape from the automated frame images, the actual time from partial penetration to complete penetration was obtained. The experimental and simulated results show that the established mathematical model can respond the change of weld penetration with varying welding electric parameters, and the effect of welding current is more apparent. The predicted results based on the established model agree well with the measurement.

Key words: gas tungsten arc welding; welding electric parameters; modeling and simulation; weld penetration

Effect of pressure and welding parameters on weld bead geometry of GMAW in underwater hyperbaric dry environment LIU Jian, XUE Long, HUANG Jiqiang, HUANG Junfen (Beijing Key Laboratory of Opto-Mechatronic Equipment Technology, Beijing Institute of Petro-chemical Technology, Beijing 102617, China). pp 29 – 32, 98

Abstract: Underwater hyperbaric welding was conducted, with the ambient pressure, welding current, composition of welding gas and electrode extension as variables, to investigate the influence on the weld bead geometry. The variation trends of weld penetration, weld width and reinforcement with the above variables were determined by orthogonal experiments. The results show that with the increase of ambient pressure, the welding spatters, weld penetration and reinforcement increased, but the weld width decreased. In hyperbaric environment, with the increase of welding current, the weld width did not change significantly, but the weld penetration increased and the reinforcement also increased slightly. With the increase of CO_2 ratio in shielding gas, the weld penetration decreased, the weld width increased, but the reinforcement had no obvious change. With the increase of electrode extension, the weld penetration decreased, the weld width and reinforcement increased.

Key words: hyperbaric welding; gas metal arc welding; weld bead geometry; spatter

Calculation method for dent strain in oil and gas pipeline WU Ying[1], JIN Pengwei[1], ZHANG Peng[1], LI Min[2] (1. School of Civil Engineering and Architecture, Southwest Petroleum University, Chengdu 610500, China; 2. Sinopec Southwest Petroleum Engineering Co., Ltd, Deyang 618000, China). pp 33 – 37

Abstract: Since the depth criterion cannot meet the demands of oil and gas industry for detecting dent defects in pipeline, a dent evaluation system based on strain was proposed in this paper. In classical shell theory, bending strain can be calculated by the values of dent depth, but the membrane strain can not be calculated by the geometric relationship between displacement and strain. In order to obtain the desired membrane strain values, arc-length method, polynomial, energy method and calculation method of membrane strain according to the bending strain were used respectively to simulate and calculate the actual membrane strain values, and compared with results from finite element calculation. It was found from the analysis and comparison that the calculated membrane strain according to bending strain was closer to actual membrane strain values, which is instructive for the use of strain criterion in evaluating integrity of dented pipeline.

Key words: dent; oil and gas pipeline; bending strain; membrane strain; finite element